

www.acsami.org Forum Article

# Thin-Film Morphology and Optical Properties of Photoisomerizable Donor–Acceptor Oligothiophenes

David M. Camero, Nathan J. Grinalds, Cory T. Kornman, Stefano Barba, Lei Li, Asmerom O. Weldeab, Ronald K. Castellano,\* and Jiangeng Xue\*



Cite This: https://doi.org/10.1021/acsami.2c05946



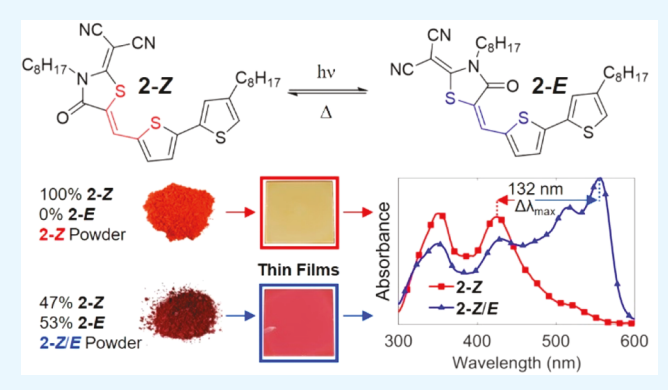
**ACCESS** I

Metrics & More

Article Recommendations

s Supporting Information

ABSTRACT: It was recently reported that the most popular electron-accepting units introduced to  $\pi$ -conjugated oligomers studied for organic photovoltaic applications are susceptible to unwanted and even destructive photochemical reactions. The consequences of Z/E photoisomerization of the popular 2-(1,1-dicyanomethylene)rhodanine (RCN) unit on the optical and morphological properties of a homologous series of RCN-functionalized oligothiophenes are studied here. Oligomers consisting of one, two, or three thiophene units were studied as pure Z isomers and with E isomer compositions of 25, 53, and 45%, respectively, for Z/E mixtures. Solutions of Z isomers and Z/E mixtures were characterized by UV-vis and photoluminescence spectroscopy, wherein changes to optical properties were evaluated



on the basis of E isomer content. X-ray diffraction of thin-film Z/E mixtures reveals crystalline domains of both Z and E forms after thermal annealing for mono- and bithiophene oligomers, with greater interplanar spacing for E crystalline domains than the Z counterparts along the substrate normal direction. The surface morphology viewed by atomic force microscopy also shows fiberlike structures for the E form with a much larger aspect ratio than for the Z domains in the bithiophene oligomer. Optical characterization reveals drastic changes in the solid state upon introduction of the E form for the mono- and bithiophene derivatives, whereas subtle consequences are noted for the terthiophene analogue. Most notably, a 132 nm redshift in maximum absorption occurs for the bithiophene oligomer films containing 53% E isomer compared to the pure Z counterpart. Finally, although solid-state photoisomerization experiments find no evidence of  $Z \to E$  isomerization in polycrystalline Z films,  $E \to Z$  isomerization is observed and becomes more restrictive in films with higher crystallinity (i.e., after thermal annealing). This structure—property study, which elucidates the consequences of the RCN configuration on solid-state packing and optical properties, is expected to guide the development of more efficient and stable organic optoelectronic devices.

KEYWORDS: conjugated molecules, donor-acceptor oligomers, dicyanorhodanine, organic photovoltaics, optoelectronic properties, photoisomerization

# **■ INTRODUCTION**

In the last two decades, there has been tremendous development in organic photovoltaic (OPV) technologies based on conjugated small molecules and polymers. The design and synthesis of a large number of photoactive organic materials have been central to the development and understanding of how molecular structures and material processing conditions impact solid-state morphology and optoelectronic properties. Covalently linking electron-withdrawing acceptor units to electron donors to form donor—acceptor oligomers or polymers has been widely explored to tune energy levels and light absorbing properties of photoactive materials. For example,  $\pi$ -conjugated molecules end-capped with electron-withdrawing units containing dicyano groups, such as 2-(1,1-dicyanomethylene)rhodanine (RCN, Figure 1a) and 2-(3-oxo-2,3-dihydroinden-1-ylidene)malononitrile (INCN) deriva-

tives, <sup>13,14</sup> have been used to great effect in this context, generating power conversion efficiency (PCE) values beyond 15% for an RCN-based all-small-molecule organic solar cell and 18% for a difluoro-substituted INCN functionalized nonfullerene acceptor (NFA)-based device, respectively. <sup>15–17</sup>

Although many of the reported small molecule donor and NFA materials demonstrate good light-harvesting properties,  $^{18,19}$  the requirement that electron-accepting units be conjugated to the  $\pi$ -backbone brings inherent weaknesses that

Special Issue: Applied Supramolecular Materials

Received: April 6, 2022 Accepted: June 15, 2022



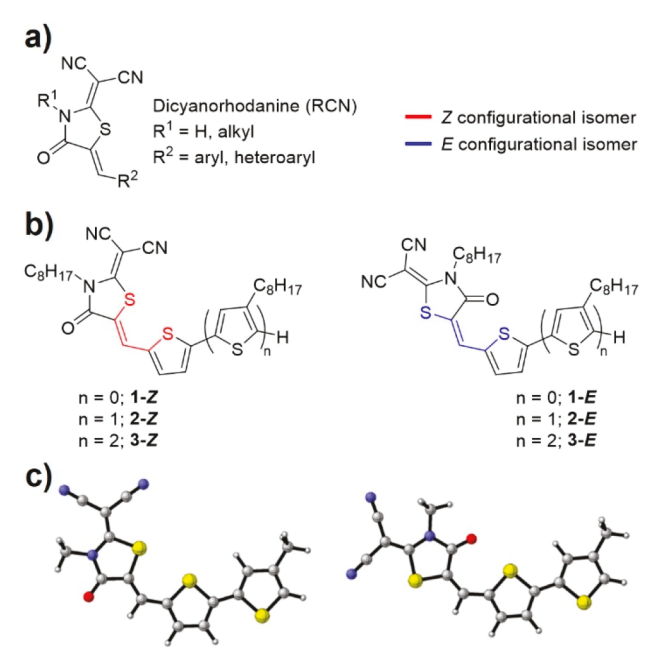


**Figure 1.** (a) Dicyanorhodanine acceptor unit; (b) chemical structures of compounds 1, 2, and 3 shown in the Z configuration (red) and the E configuration (blue); and (c) representative optimized geometries at the B3LYP/6-31+G(d) level for 2-Z, left, and 2-Z, right (gas-phase, all octyl chains were truncated to methyl groups to reduce computational cost).

have only recently come to light. The exocyclic double bond often employed to conjugate electron-deficient units to a  $\pi$ -conjugated backbone is the culprit of various unanticipated photochemical reactions that provide nonradiative deactivation pathways from electronically excited states,  $^{20-22}$  in direct competition with the exciton charge separation required to generate electrical current.  $^{23}$  Molecules can be designed with  $\sigma$  bond linkages between donor—acceptor motifs, thereby lacking exocyclic olefin photoisomerization pathways, such as diketopyrrolopyrrole (DPP)-based conjugated materials.  $^{24}$  However, olefin conjugation is required for RCN- and INCN-functionalized materials,  $^{25,26}$  which comprise state-of-the-art OPVs.  $^{5,6,27}$ 

Recently, our lab reported the solution Z/E photoisomerization of RCN-functionalized thiophenes wherein it was discovered that these systems undergo well-behaved, reversible double-bond isomerization under ultraviolet (UV) and visible-light irradiation to yield distributions of Z and E isomers at the photostationary state. Shortly after, two separate reports identified similar photochemical reactions demonstrating that INCN-functionalized oligomers can undergo tandem isomerization—electrocyclization reactions and/or isomerization—epoxidation reactions under certain irradiation conditions.

It is important to recognize that unintentional photochemical reactions result in changes to the chemical structure of the photoactive molecules and, within this sector of the organic materials community, it is well-appreciated that small changes in chemical structure may result in rather significant changes in optoelectronic properties and photovoltaic device performance. <sup>29–31</sup> For example, it has been shown recently that altering the structural connectivity of INCN-functionalized fused-ring electron acceptors (FREAs) can result in a nearly 30% increase in overall OPV device efficiency. <sup>32</sup>

Similarly, adjusting alkyl group placement from parato meta-substitution resulted in a measurable increase in PCE for an INCN-functionalized NFA used in polymer solar cells. Certainly, the links between molecular structure and thin-film morphology are understood to have an important impact on the optical properties and optoelectronic performance of organic-based devices; 4-36 however, it is also well-accepted that controlling solid-state organization remains an interesting challenge. At the same time, photoisomerization is known to result in appreciable changes in solid-state morphology characteristics, which in turn can have concomitant impacts on downstream optical and electronic properties critical to OPV device performance.

Conversely, photoactive units are often used intentionally to modulate optical properties for applications in photoresponsive smart materials. For instance, photolabile diarylethenes (DAEs) have been used to great effect for this purpose, contributing to the next generation of organic soft materials ranging from photoresponsive transistor display materials to smart anticounterfeiting ink technologies. In addition, the photoswitchable isomerization in azobenzene has been leveraged to develop photoresponsive dynamic materials such as hydrogels. Clearly, more work is required to understand the incorporation of electron-accepting units conjugated by photolabile double bonds and the impacts this might present on the solid-state structure and optoelectronic properties relevant to their functionality in OPV devices.

Although our initial work was aimed at characterizing the photochemical reactions of RCN-functionalized thiophenes in solution, <sup>25</sup> reported here is an extension of the study to the solid state to systematically assess the optoelectronic and morphological properties of isomeric mixtures achieved via photoisomerization. Although solid-state investigations and the resulting impacts on device performance have been considered previously for photolabile INCN-functionalized thiophenes regarding tandem isomerization—electrocyclization and epoxidation reactions, <sup>26,28</sup> there are no reports to the best of our knowledge of how modulating RCN stereochemistry via controlled  $Z \rightarrow E$  isomerization reactions affects optoelectronic and morphology characteristics in powders and thin films.

Herein, we report our investigations of photoisomerizable RCN-functionalized oligothiophenes in the solid state, and the impact of modulating isomeric compositions on morphological and thin-film optoelectronic properties. Three relatively simple model compounds of varying oligothiophene length were chosen, eliminating extraneous variables associated with processing and characterization of more complex chemical structures. This work aims to delineate trends for these photoisomerizable RCN-functionalized oligothiophenes as they might apply to more complex electronic materials.

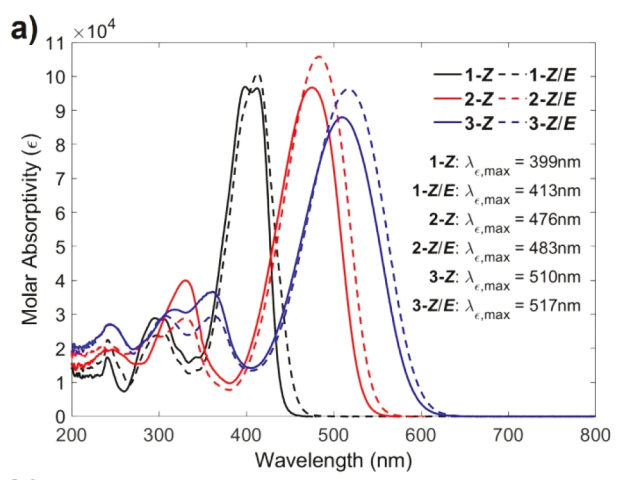
Specifically, three RCN-functionalized model substrates ranging from one to three thiophene units comprising the  $\pi$ -conjugated backbone have been synthesized (Figure 1b). Compounds 1, 2, and 3 were isolated as the thermodynamically stable Z isomers, in agreement with the literature precedent. To mimic the effects of unintentional irradiation resulting in the introduction of Z/E isomeric mixtures into downstream processing events, we performed large-scale photoisomerization reactions starting with 1-Z, 2-Z, and 3-Z to yield gram amounts of three unique isomeric mixtures (1-Z/E, 2-Z/E, and 3-Z/E), which were compared directly to the corresponding Z isomer samples for the studies discussed herein. The isomeric compositions consisted of 25, 53, and

45% E isomer for the 1-Z/E, 2-Z/E, and 3-Z/E mixtures, respectively. The optoelectronic properties of Z isomers and Z/E mixtures were assessed in solution by ultraviolet-visible (UV-vis) and photoluminescence (PL) spectroscopy. Solution Z/E mixtures exhibited increased molar absorptivity, decreased PL intensity, and small (<15 nm) redshifts in absorbance/emission. Because the individual E isomers for RCN-functionalized thiophenes are not easily separable by conventional means, 25,49 compounds 1-3 were modeled by ground-state density functional theory (DFT) calculations. Computationally derived absorption profiles of the Z and E isomers from time-dependent (TD) methods support the observed trends. The thermal stabilities of Z isomer samples and corresponding Z/E mixtures were analyzed by thermogravimetric analysis (TGA) and differential scanning calorimetry (DSC) prior to solution processing into thin films and subsequent thermal annealing studies.

Z isomers and Z/E mixtures of 1, 2, and 3 were solution processed into thin films by spin coating to allow surface morphology and crystal structure characterization using atomic force microscopy (AFM) and X-ray diffraction (XRD), respectively. Solid-state absorbance and PL measurements were conducted using films processed from both pure Z isomer samples and solid-state Z/E mixtures, where it was found that mono- and bithiophene derivatives underwent notably more dramatic optical changes compared to the terthiophene Z and Z/E mixtures. Postdeposition thermal annealing of the thin films was found to drive further crystallization, resulting in more ordered and tightly packed crystalline domains. This was accompanied by the emergence or intensification of longwavelength shoulder peaks in the absorption spectra and a drastic increase in PL intensity for films containing Ecrystallites. Finally, solid-state isomerization experiments were conducted with 2-Z and 2-Z/E thin films under irradiation with multiple visible-light sources. It was found that pure 2-Z film composition remains unaffected after prolonged visible irradiation, whereas changes in the Z/E isomeric ratio were observed for the 2-Z/E films, indicating  $E \rightarrow Z$  isomerization in the solid state. The solid-state photoisomerization is an important consideration when handling RCN-based thin films under practical conditions. Although the solution photoisomerization behavior of RCN-functionalized thiophenes has been previously characterized, potential consequences of this process on solid-state optoelectronic and morphological characteristics are of broader impact to the OPV community, and the results of this work will be of particular relevance to practitioners in this field.

# ■ RESULTS AND DISCUSSION

**Optical Properties in Solution.** The intrinsic optoelectronic properties of each Z isomer were characterized as  $20~\mu\mathrm{M}$  solutions in chloroform by UV–vis spectroscopy. The absorbance profile of compounds 1-Z and 2-Z have been reported previously in chloroform,  $^{25}$  and show primary  $\lambda_{\mathrm{max}}$  absorbance bands centered at 399 and 476 nm, respectively, whereas the newly added compound 3-Z displays a further redshifted  $\lambda_{\mathrm{max}}$  absorbance at 510 nm (Figure 2a). Irradiation of each solution to a photostationary state reveals common trends for each sample; a slight redshift in  $\lambda_{\mathrm{max}}$  accompanied by an increase in peak absorbance value was observed upon irradiation, resulting in  $\lambda_{\mathrm{max}}$  values of 413, 483, and 517 nm for 1-Z/E, 2-Z/E, and 3-Z/E, respectively (Figure 2a). For all compounds, the maximum molar absorptivity was observed in



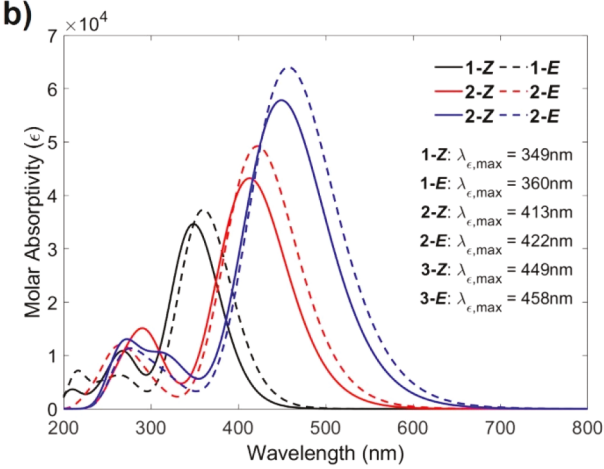


**Figure 2.** (a) Solution UV—vis absorption spectra of 20  $\mu$ M 1-Z, 2-Z, and 3-Z (solid lines) in chloroform and corresponding Z/E mixtures (dashed lines) upon irradiation to a photostationary state. (b) Time-dependent DFT absorption profiles for Z and E isomers of 1, 2, and 3 (CAM-B3LYP/cc-pvdz).

the visible spectrum, corresponding to the first excited-state optical transition (i.e., intramolecular charge transfer state of the donor-acceptor oligomer). Absorption peaks in the UV region are attributed to a combination of various excited-state transitions that are more localized within the donor or the acceptor moieties. This was confirmed from gas phase TD-DFT calculations (Tables S2-S6). The experimental results in chloroform are in excellent agreement with the absorbance profile trends obtained from TD-DFT calculations at the CAM-B3LYP/cc-pvdz level of theory (Supporting Information, page S22). A 9-11 nm redshift was calculated for structures optimized in the E configuration compared to the corresponding Z form, accompanied by an increase of 8-14% in the maximum molar absorptivity  $(\varepsilon_{\text{max}})$  for the E isomer (Figure 2b). The TD-DFT calculated  $\lambda_{max}$  for 1-Z was predicted to be 349 nm in the gas phase compared to 360 nm for 1-E. The predicted peak absorbance for 2-Z and 2-E was at wavelengths of 413 and 422 nm, respectively, compared to 449 and 458 nm for 3-Z and 3-E, respectively.

Solution UV—vis and PL spectra are displayed together for the mono-, bi-, and terthiophene oligomer solutions to draw comparisons between Z and E isomer optoelectronic properties (Figure 3). The 1-Z and 1-Z/E solutions exhibit similar molar absorptivity and PL profiles. However, the 1-Z visible

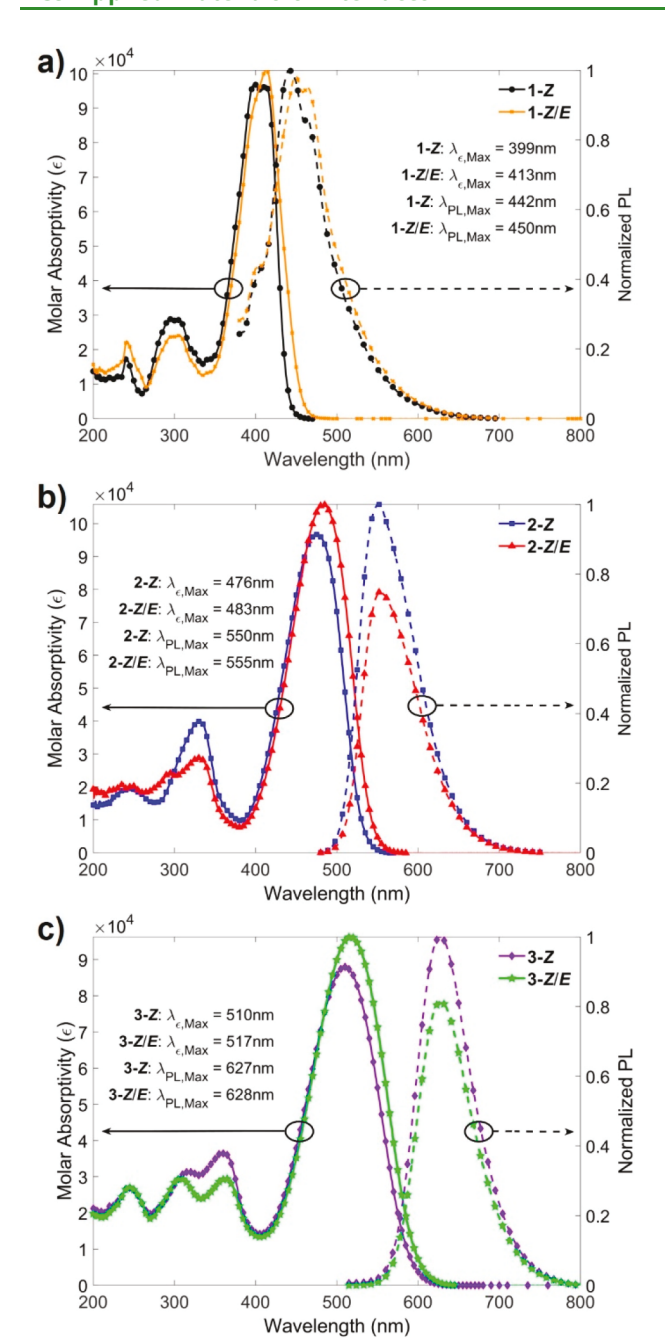


**Figure 3.** Optical properties of 20  $\mu$ M RCN compounds dissolved in chloroform. Molar absorptivity ( $\varepsilon$ ) and normalized photoluminescent (PL) intensity is plotted for (a) 1-Z and 1-Z/E, (b) 2-Z and 2-Z/E, and (c) 3-Z and 3-Z/E. The PL is taken at excitation wavelengths of 375, 475, and 510 nm for compounds 1, 2, and 3, respectively. PL is also normalized by absorptance at the excitation wavelength and to global maximum emission among the pure compound and its isomeric mixture.

peak contains two distinct optical transition, whereas the 1-Z/E spectrum has a single maximum caused by the overlapping and slightly red-shifted optical response of the E-isomer (Figure 3a). The 412 nm 1-Z peak is assigned as the 0–0 transition of the first excited state. The 1-Z  $\lambda_{\text{max}}$  occurs at 399 nm and is assigned as the 0–1 transition with phonon coupling of  $\sim$ 0.1 eV. The 1-Z/E spectral response has  $\lambda_{\text{max}}$  red-shifted by 14 nm owing to the 0–0 transition of the 1-E molecules. Comparing 0–0 transitions for the 1-E and 1-E0 solution,

only a 1 nm redshift was observed. Additionally, a 3% increase in  $\varepsilon_{\rm max}$  was observed for the 1-Z/E solution.

The PL spectra of the 1-Z and 1-Z/E mixtures were measured at an excitation wavelength ( $\lambda_{\rm exc}$ ) of 375 nm. The PL spectra display a nonzero baseline for the low wavelength tail. This stems from overlapping dual fluorescent emission observed in 1-Z and 1-Z/E solutions, indicated by emission well below wavelengths associated with the first excited state (Figure S14). Mechanisms for single-molecule dual fluorescence are still debated and several possibilities exist. Because of the photoinduced bond rotations for these D–A molecules, a twisted intramolecular charge transfer (TICT) mechanism is most likely responsible. S0,51 Although dual fluorescence is not the focus of this study, it explains the nonzero baseline pertaining to the high energy side of the PL spectra in the 1-Z and 1-Z/E compounds.

The fluorescence shows a peak PL intensity at 441 and 450 nm for 1-Z and 1-Z/E solutions, respectively. Only a 2 nm redshift was observed for the 465 nm PL vibronic peak and the emission tails are almost identical traces. Taking the Stokes shift  $(\Delta \lambda_{\rm Stokes})$  as the differences between maxima of the first excited-state transitions,  $\Delta \lambda_{\rm Stokes}$  was measured to be 42 and 37 nm for 1-Z and 1-Z/E, respectively. UV—vis and PL spectra confirm small changes to intramolecular optical transitions for 1-E molecules. Additionally, the mixture is comprised of 25% E isomers, so the Z to E spectral changes were diluted by the large Z isomer concentration.

The molar absorptivity and PL for 2-Z and 2-Z/E (Figure 3b) and 3-Z and 3-Z/E (Figure 3c) compounds show similar behavioral trends. As additional thiophenes are added,  $\lambda_{\rm max}$  is red-shifted because of the increased delocalization of  $\pi$ -electrons. The 2-Z  $\lambda_{\rm max}$  occurs at 476 nm. A 7 nm redshift and 9% increase in  $\varepsilon_{\rm max}$  is also observed for the 2-Z/E solution. The PL spectra show a 5 nm redshift for the 2-Z/E mixture along with 26% less integrated intensity. There is a 74 and 72 nm  $\Delta\lambda_{\rm Stokes}$  for the 2-Z and 2-Z/E solutions. The  $\lambda_{\rm max}$  is further red-shifted for the 3-Z and 3-Z/E solutions, to 510 and 517 nm, respectively. 3-Z/E possesses a 1 nm red-shifted peak emission wavelength and 20% decrease in PL efficiency compared to 3-Z. Larger  $\Delta\lambda_{\rm Stokes}$  occurs for the 3-Z and 3-Z/E solutions at 117 and 111 nm, respectively.

The geometric isomers exhibit mostly modest changes to their allowed optical transitions in solution. In each case, the E isomer exhibits increased molar absorptivity, decreased PL intensity, red-shifted absorbance/emission, and decreased  $\Delta \lambda_{\text{Stokes}}$ . Some of these changes may be desirable, such as an  $\varepsilon_{
m max}$  increase. Increased molar absorptivity offers benefits to applications like OPVs where RCN acceptor units are commonly employed. However, optical properties of individual molecules seen in solution do not solely dictate their solid-state behaviors. Molecules are sensitive to their nearest-neighbor environment, and intermolecular coupling can cause new optical transitions to emerge.<sup>35</sup> On the basis of the configurational change of these isomers, different molecular packing may be expected. Therefore, the remainder of this work investigates solid-state structural and optical behavior comparisons between these stereoisomers. This work serves as an example for other RCN-functionalized thiophenes used in solid-state devices.

Morphology and Molecular Packing of Thin Films. Thin films were solution processed in a glovebox via spin coating at a concentration of 30 mg/mL in chlorobenzene at 2000 rpm. These films were spun on glass substrates coated

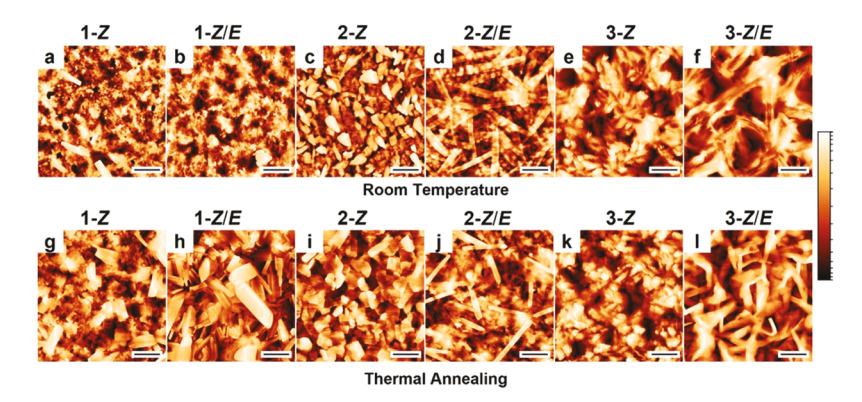


Figure 4. AFM height images of 1-Z, 1-Z/E, 2-Z, 2-Z/E, 3-Z, and 3-Z/E thin films, fabricated at room temperature (top panel) and after thermal annealing (bottom panel). Height color-bar scale range is (a-d) 80, (e-h) 50, and (i-l) 140 nm. Scale bar insets are (a-h) 1, (i-k) 2, and (l) 4  $\mu$ m.

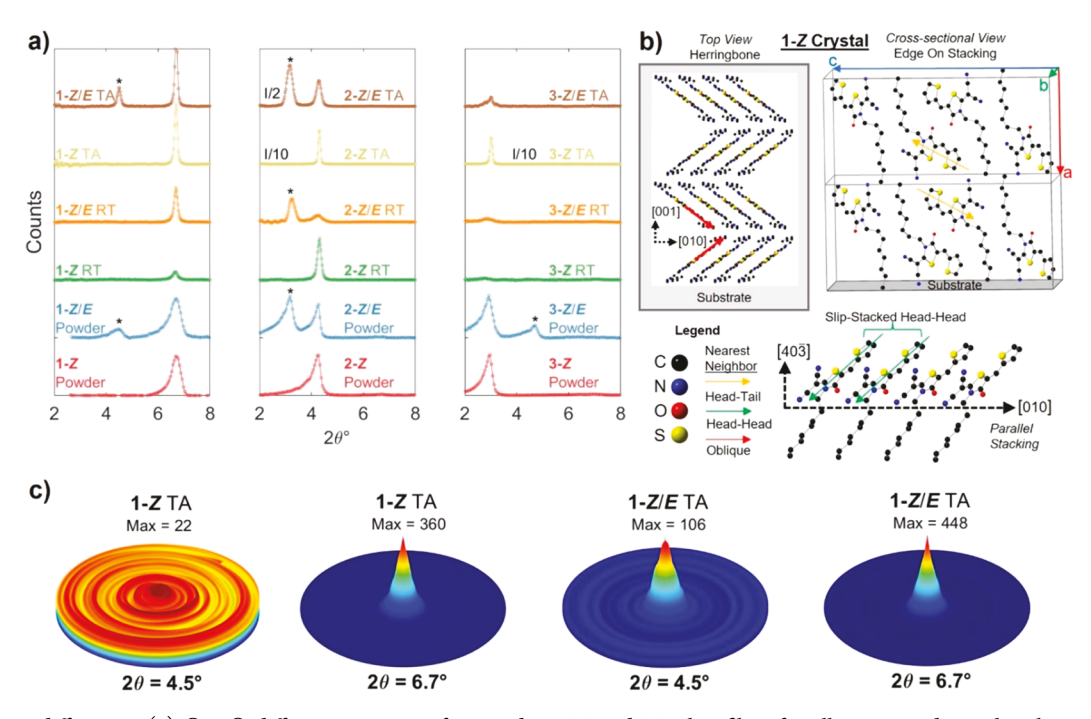


Figure 5. X-ray diffraction. (a)  $\Theta$ –2 $\Theta$  diffraction patterns for powder, RT, and TA thin films for all compounds. Each column shows data for samples with the same thiophene units. Diffraction associated with *E* isomer crystal planes is labeled with a star. (b) 1-*Z* single-crystal molecular packing is viewed relative to its substrate in a top view (left) demonstrating long-range herringbone ordering. A cross-sectional view (right) of two vertically stacked unit cells displays the edge-on stacking behavior relative to the substrate. Finally, an additional viewing direction of slip-stacked parallel packing is shown (bottom). Examples of nearest-neighbor molecular orientations are labeled by colored arrows, with each viewing direction illustrating nearest-neighbor orientations present in 1-*Z* crystals. (c) Pole figure plots for 1-*Z* TA and 1-*Z*/*E* TA films with 2Θ = 4.5° (for *E* crystallites) and 2Θ = 6.7° (for *Z* crystallites). The maximum signal is reported in counts for each plot.

with poly(3,4-ethylenedioxythiophene) polystyrenesulfonate (PEDOT:PSS) to improve wettability. TGA and DSC were performed using pure Z isomers and Z/E mixtures to assess the thermal stability of these compounds during thermal annealing (TA) studies (Figures S6 and S19–S22). DSC indicates melting temperatures ranging from 110–150 °C depending on the compound. Therefore, the 90 °C TA kept films limited to the solid state. In addition, thermally annealed films were analyzed by ¹H NMR to verify the structural integrity (Figures S7–S8). Films fabricated at room temperature (RT) were characterized, alongside films with postdeposition thermal annealing (TA) at 90 °C for 1 h. Atomic force microscopy (AFM) and X-ray diffraction (XRD) characterization methods were employed to investigate surface morphology and crystal

packing for the thin films. These techniques reveal the consequences of isomerization on surface and bulk structures, providing insight into optical properties discussed later.

All compound microstructure images were obtained with AFM for RT and TA films (Figure 4). The 1-Z RT (Figure 4a) and 1-Z/E RT (Figure 4b) films show similar disordered textures. A few larger grains approximately 1  $\mu$ m in length were seen for both films. Close inspection of the disordered regions reveals nucleation of small grains among the amorphous film. The 1-E isomer does not appear to significantly impact the morphology during the initial deposition. Mobility provided from TA enables molecular reorganization into crystalline regimes. Consequently, larger and less amorphous microstructures emerge. The 1-Z film after TA (Figure 4g) contains

Table 1. X-ray Diffraction Θ−2Θ Data Summary

sample	Z-crystallite $(2\theta^{\circ})$	E-crystallite $(2\theta^{\circ})$	$d_Z$ (Å)	$d_E$ (Å)	crystallite size $ au_Z$ (nm)	crystallite size $\tau_E$ (nm)
1-Z Powder	6.72		13.1		20	
1-Z/E Powder	6.70	4.46	13.2	19.8	17	18
1-Z RT	6.65		13.3		39	
1-Z/E RT	6.68		13.2		52	
1-Z TA	6.69		13.2		66	
1-Z/E TA	6.69	4.5	13.2	19.6	73	56
2-Z Powder	4.24		20.8		23	
2-Z/E Powder	4.25	3.17	20.8	27.8	30	18
<b>2-</b> Z RT	4.31		20.5		48	
<b>2-</b> Z/E RT	4.25	3.24	20.8	27.2	18	34
<b>2-</b> Z TA	4.30		20.5		93	
<b>2-</b> Z/E TA	4.29	3.16	20.6	27.9	41	34
3-Z Powder	2.95		29.9		24	
3-Z/E Powder	2.93	4.62	30.2	18.8	17	19
3-Z RT	2.78		31.8		20	
<b>3-</b> Z/E RT	2.83		31.2		16	
3-Z TA	3.02		29.2		83	
3-Z/E TA	2.99		29.5		33	

large platelet-shaped grains among smaller platelets and irregular grains. Larger grains are present in the annealed 1-Z/E film, although no obvious features are clearly unique to the 1-E molecules (Figure 4h).

Microstructure differences are highly apparent between the 2-Z and 2-Z/E films (Figure 4c, d, i, j). The microstructure of the 2-Z RT film contains amorphous domains alongside platelet and wedge-shaped grains (Figure 4c), whereas the 2-Z/E RT film (Figure 4d) does not contain wedge-shaped domains. Instead, highly disordered fiber grains are identified by their large aspect ratio. This fiber morphology is attributed to the E isomer, a claim further supported by XRD (vide infra). These fibers are a few micrometers long and possess height differences along their length.

The data suggest many molecules have not migrated to equilibrium positions along the fiber domains. The 2-Z TA thin films (Figure 4i) displayed well-defined grains and an absence of amorphous zones. Annealing the 2-Z/E film enables migration to more ordered fiber domains, eliminating large height variation along their lengths (Figure 4j). Additionally, a distinct phase separation of fiber and platelet shapes are present for 2-Z/E TA. The Z isomer grains in the 2-Z/E TA thin film are much smaller than those in 2-Z TA.

A primarily amorphous texture is present for the 3-Z and 3-Z/E RT films (Figure 4e, f). Micrometer-sized grains are seen for the 3-Z TA film (Figure 4k), whereas the 3-Z/E TA film (Figure 4l) forms a large, branched network. Because many organic devices rely on materials interfaces, the large microstructural differences between Z and Z/E films could impact downstream device metrics, such as interfacial charge separation and charge transport. The 3-Z/E TA film does not provide evidence of separate E and Z domains as is the case with the Z-Z/E film.

XRD studies were used to investigate the crystalline packing of the Z and E isomers. XRD  $\Theta$ - $2\Theta$  scans for the compounds as powders and thin films are shown in Figure 5a and relevant quantitative information is summarized in Table 1. Diffraction was only observed in the  $2\Theta$  range of 2– $8^{\circ}$  for all thin-film samples. Although Z isomer powders exhibit a single peak within this scan range, the Z/E powders exhibit an additional peak associated with the E isomer crystallites. The exact crystal

structure for all powders and thin films could not be obtained. However, a single-crystal diffraction pattern of the 1-Z compound was measured in a previous study.<sup>25</sup> This information was used to construct a monoclinic unit cell with  $\beta = 90.13^{\circ}$  and lattice parameters of 13.4, 5.5, and 24.64 Å for a, b, and c, respectively. The 1-Z unit cell contains four molecules engaged in herringbone packing (Figure 5b). The 1-Z crystallite diffraction occurs at a 2 $\Theta$  value of  $\sim$ 6.7 $^{\circ}$  and therefore, has Z crystallite interplanar spacing  $(d_Z)$  of 13.2 Å. The agreement between  $d_7$  for the 1-Z powder and the single crystal 1-Z a lattice parameter (13.4 Å) suggests the thin film and powder diffraction of Z crystallites corresponds to the (100) plane. The 1-Z/E powder shows an additional diffraction peak at 4.46°, corresponding to an interplanar spacing  $(d_E)$  of 19.8 Å for E crystallites. This peak is not present in the 1-Z/E film prepared at RT but emerges in the annealed film that is consistent with molecular ordering evidenced from the AFM images. Increased crystallinity with TA is reflected by the increased counts relative to their RT counterparts. Only one diffraction peak was observed for each crystallite in the thin film. This is attributed to the preferred molecular orientation on the substrate surface, further confirmed with pole figure measurements for the 1-Z TA and 1-Z/E TA films (Figure 5c).

The leftmost pole figure intensity plot displays data for the 1-Z film at the suspected E crystallite diffracting plane (2 $\Theta$ value of 4.5°) with varying sample tilt and azimuthal angle at 5° increments. Negligible signals (maximum counts = 22) are recorded throughout the scan, confirming that the 1-Z film does not possess the E-crystallite peak at any orientation. The pole figure for the TA 1-Z film at  $2\Theta$  of  $6.7^{\circ}$  shows maximum signal at zero sample tilt. Therefore, molecular alignment of the (100) planes is preferred parallel to the sample surface, suggesting an edge-on stacking configuration for the oligomers in the thin films. The preferred stacking direction of the Z crystallites is demonstrated in both the top-down and crosssectional viewing directions in reference to the substrate surface (Figure 5b). The long-range herringbone structure and oblique nearest-neighbor molecular arrangements can be seen in the top viewing direction in Figure 5b. The head-to-tail (HT) nearest-neighbor arrangement can be seen in the crosssection diagram of two-unit cells vertically stacked with an HT pair outlined by orange arrows. Additionally, a slip-stacked head-to-head (HH) nearest-neighbor orientation is seen along the [010] direction in the bottom diagram. For the annealed 1-Z/E film, pole figures also reveal that (100) planes in the 1-Z domains remain parallel with the surface; furthermore, the 1-Z crystal planes responsible for diffraction also preferentially orient parallel to the surface.

XRD of the 2-Z and 3-Z powders reveal interplanar spacing of  $d_Z=20.8$  and 29.9 Å, respectively, showing an increase in 7.6 and 16.7 Å compared to  $d_Z$  for 1-Z. These differences are approximately twice the length from thiophene unit(s) added to the donor moiety for 2-Z and 3-Z, which are 3.9 and 7.8 Å, respectively, compared to 1-Z. This is consistent with the herringbone structure of these materials, in which two molecules are essentially aligned in the [100] direction with the HT nearest-neighbor configuration (see Figure 5b).

The  $\Theta$ -2 $\Theta$  scan for the 2-Z and 2-Z/E films show somewhat different behavior to 1-Z and 1-Z/E. The 2-Z RT film contains a single peak associated with 2-Z crystallites, whereas the RT 2-Z/E film shows two peaks, corresponding to separate Z and E domains. The diffraction peak at  $2\Theta = 3.2^{\circ}$  is attributed to 2-E domains, corresponding to the fiber microstructures observed in AFM (Figure 4d). The diffraction intensity increased after TA, suggesting a higher crystallization order after the heat treatment. Interestingly, the 2-Z TA film also had a 3-fold higher signal compared to the 2-Z/E TA film when normalized for Z isomer concentration differences. Additionally, the mean Z crystallite size  $(\tau_7)$  from Scherrer's equation is 93 nm for the 2-Z TA film compared to 41 nm for the 2-Z/E TA film, suggesting that the presence of 2-Emolecules in the 2-Z/E mixture inhibits Z crystallite growth to some extent. The larger platelet grains in the 2-Z TA film compared to platelets of 2-Z/E TA support this observation (Figure 4i–j). Pole figures scans were also taken for 2-Z and 2-Z/E and show a similar preferred packing orientation to the 1-Z and 1-Z/E crystallites (Figures S14 and S15).

The amorphous nature of the 3-Z RT and 3-Z/E RT films is reflected in the extremely weak diffraction signals at  $2\Theta=2.9^\circ$ , which correspond to approximately 1.5 Å greater  $d_Z$  than that for the powders. This may be due to steric hindrance of the additional solubilizing chains (one octyl chain on each additional thiophene unit) limiting molecular packing. As thermal energy is provided, Z crystallites emerge in large quantity for the 3-Z film, while less crystal growth is observed in the 3-Z/E TA film. Again, E isomers inhibit crystal packing of Z isomers. Nevertheless, with the increased degrees of crystallization in the TA films,  $d_Z$  is slightly reduced back to the values for the powders. No evidence of E crystallite formation was found in either 3-Z/E RT or TA films.

Single crystals of pure E isomers were not obtained because of photoisomerization limits that inevitably lead to inseparable  $\mathbb{Z}/E$  mixtures. However,  $\mathbb{I}\text{-}Z/E$  and  $\mathbb{I}\text{-}Z/E$  compounds show  $\sim$ 7 Å greater interplanar spacing for E domains compared to E domains. We hypothesize that these E domains have similar overall packing structure as the E domains, with the main difference arising from the thiophene-olefin bond orientation altering lattice parameters. However, the  $\mathbb{I}\text{-}Z$  and  $\mathbb{I}\text{-}Z$ -crystallite behavior. The  $\mathbb{I}\text{-}E$ -crystallite interplanar spacing observed from the powder samples is smaller than that for the E-crystallite suggest isomerization can cause rather significant changes to

crystal packing, which may subsequently influence optoelectronic properties.

In summary, a herringbone pattern was assigned to the 1-Z crystallites by comparison to single-crystal XRD data. Interplanar spacing for the 2-Z and 3-Z crystallites are within reasonable agreement of thiophene additions to the known unit-cell geometry. Therefore, similar herringbone structures are likely present in the Z configuration for all compounds. E crystallites possess unknown unit cells but are shown to have larger d-spacing for 1-E and 2-E crystallites. Both Z and E isomers exhibit preferred thin-film crystal growth orientation in one dimension. Z crystallites were observed in all films, whereas E crystallites required thermal energy to form in the 1-Z/E film and were not observed in any 3-Z/E films. Thin-film optical properties are subsequently explained by these solid-state morphological differences.

Optical Properties of Thin Films. Thin-film UV—vis spectroscopy and PL were measured for all compounds (Figure 6) and important parameters are summarized in Table 2. The 1-Z RT absorbance plotted in Figure 6a exhibits a wavelength of maximum absorbance ( $\lambda_{\text{max,A}}$ ) at 392 nm. This translates to a 7 nm blue shift for the liquid-to-solid-state  $\lambda_{\text{max,A}}$  change ( $\Delta A_{\text{L/S}}$ ). Increasing 1-Z crystallite concentration further blueshifts  $\lambda_{\text{max,A}}$  as observed for the 1-Z TA sample. Additionally, the oscillator strength at  $\sim$ 407 nm decreases upon annealing and is attributed to a loss of amorphous phase, whereas the 353 nm peak has an increased oscillator strength. A shoulder at 431 nm is also present in the 1-Z film, which corresponds to a 20 nm redshift compared to the solution 0–0 peak.

The 1-Z/E RT film has a similar absorbance profile to the 1-Z RT film. The change in  $\lambda_{\max,A}$  between the 1-Z/E RT and 1-Z RT film ( $\Delta A_{Z/E}$ ) is a 6 nm blueshift. This is explained by increased Z crystallite formation evident from XRD. A larger  $\Delta A_{L/S}$  is observed for the 1-Z/E RT film with a 27 nm blueshift. Absorbance profiles of 1-Z and 1-Z/E thin-film mixtures exhibit larger differences after thermal annealing. The 1-Z/E TA  $\lambda_{\max,A}$  occurs at 383 nm compared to 353 nm for the 1-Z TA film. Perhaps most intriguing is the emergence of a sharp, long wavelength peak at ~473 nm. Considering the 1-E crystallite formation in the 1-Z/E TA film as revealed by XRD, we attribute this peak to an optical transition within the 1-E crystalline domains.

The PL spectra shows significant difference between the RT and TA films for both 1-Z and 1-Z/E. The 1-Z/E RT film shows reduced overall PL intensity compared to the 1-Z RT film. Thermal annealing results in a 2.2-fold increase in PL intensity for the 1-Z film and a much larger 4.8-fold increase for the 1-Z/E film. Moreover, in the short-wavelength region of the PL spectra, the annealed 1-Z/E film possess a very strong peak at ~485 nm compared to a relatively weak shoulder at ~465 nm for the annealed 1-Z film. Consistent with the analysis of the absorption spectra, we attribute this shortwavelength peak in the 1-Z/E TA film to PL from Ecrystallites. This also contributes to the 6 nm blue shift in the peak wavelength for PL  $(\lambda_{\text{max,PL}})$  as compared to the 1-Z TA film. Also, the Stokes shift  $(\Delta \lambda_{\text{Stokes}})$  for the 1-Z/E TA spectrum is 131 nm compared to 167 nm in the 1-Z TA film, indicating changes to optoelectronic transitions associated with the *E*-isomer in the solid state.

Significantly more pronounced isomer dependence on solidstate optical properties was observed for the 2-Z and 2-Z/E thin films (Figure 6b). All 2-Z and 2-Z/E films display a high

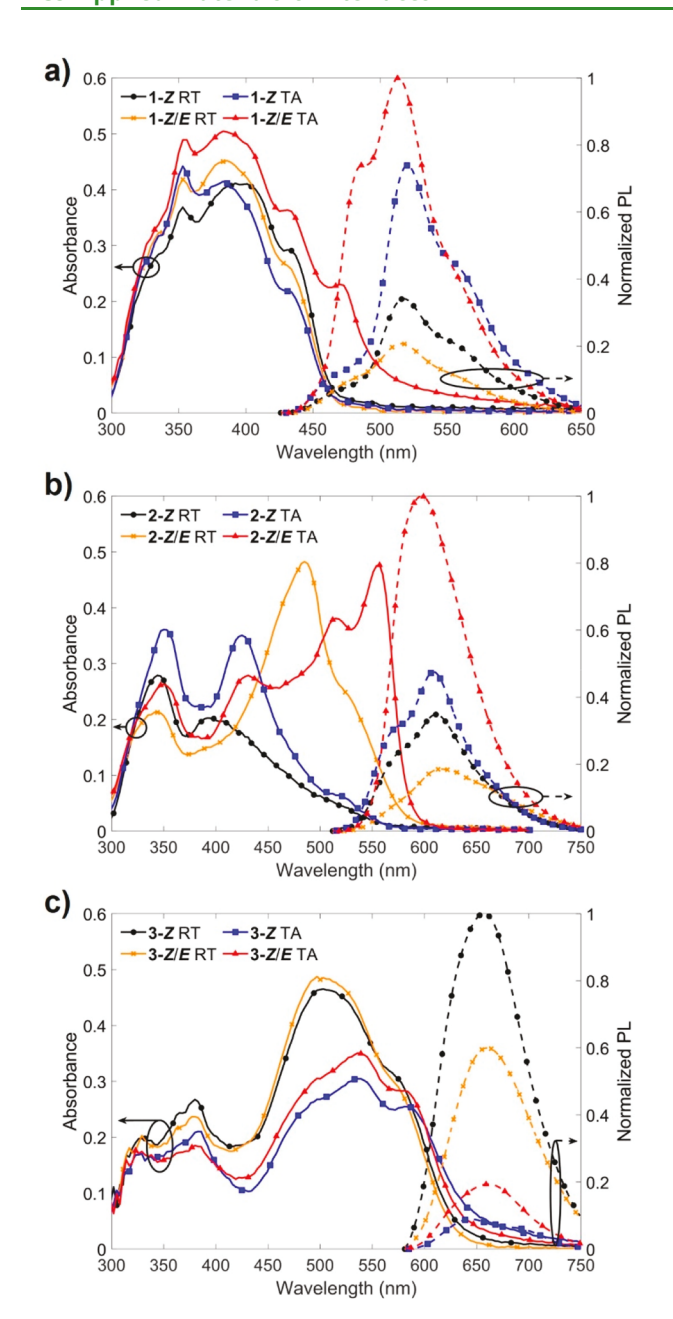


**Figure 6.** UV—vis absorption (solid lines) and the normalized photoluminescence (PL, dashed lines) spectra for room temperature spin-coated (RT) and thermally annealed (TA) films for (a) 1-Z and 1-Z/E, (b) 2-Z and 2-Z/E, and (c) 3-Z and 3-Z/E compounds. Excitation wavelengths of 360, 420, and 515 nm were used for compounds 1, 2, and 3, respectively.

energy peak at ~350 nm. Absorbance at this wavelength was seen in both solutions (Figure 3b) and attributed to higher energy excited states that are primarily localized on the RCN acceptor unit. 2-Z RT and 2-Z TA films have the strongest absorbance at high energy transitions with absorption maxima located at 344 and 350 nm, respectively. The 2-Z RT absorbance is significantly blue-shifted from its solution spectra, with the first excited-state  $\lambda_{\rm max,A}$  occurring at 392 nm. Absorbance at the solution  $\lambda_{\rm max,A}$  of 476 nm is comparatively suppressed, and a weak shoulder extends the 2-Z RT absorption edge beyond 550 nm. The 2-Z TA film has a 33 nm red-shifted  $\lambda_{\rm max,A}$  at 425 nm for its low energy

transition compared to 392 nm for the RT film. Additionally, the oscillator strength across all wavelengths increased after thermal annealing.

Introduction of the E-isomer led to a markedly different optical response with a  $\lambda_{\text{max},A}$  at 485 nm for the 2-Z/E RT film, corresponding to a rather dramatic  $\Delta A_{Z/E}$  of 93 nm. Although the 2-Z/E RT  $\lambda_{max,A}$  is only red-shifted 2 nm from the solution  $\lambda_{\text{max},A}$ , the solid-state absorption possesses a shoulder peak at ~530 nm and extends well beyond the solution absorption limit of  $\sim$ 550 nm. The main long-wavelength 2-Z/E RT film absorption feature at 485 nm is attributed to the amorphous E domains as supported by the relatively low XRD intensity and disordered texture seen in AFM, whereas the strong shoulder at  $\sim$ 530 nm is attributed to *E*-crystallites. Annealing the 2-Z/Efilm promotes Z and E crystallite formation and grain growth. This enables the strong Z crystallite optical transition at 425 nm. It also promotes stronger response from ordered E domains, resulting in a strong, long-wavelength absorption peak centered at 557 nm. Similar to the 1-Z/E TA film, the heat treatment also results in increased fluorescence intensity from both 2-Z and 2-Z/E films, especially the latter, which saw a 5.4-fold increase in PL intensity after thermal annealing. Again, a decreased Stokes shift was also associated with the presence of the E-isomer. Most significant, there is a 132 nm  $\Delta A_{Z/E}$  between the 2-Z/E TA and 2-Z TA films because of the different optical response of Z and E stereoisomers in the solid

The 3-Z and 3-Z/E films show minimal difference in their optical absorption behavior (Figure 6c). The RT films are almost entirely amorphous and have a  $\lambda_{max,A}$  of 503 and 497 nm for the Z and Z/E mixture, respectively. A shoulder is present at ~580 nm for the RT films, which becomes more pronounced upon thermal annealing. Annealing also leads to decreased absorption around the main peak center at ~500 nm, causing an apparent redshift of  $\lambda_{\text{max,A}}$  to 536 nm. A slight redshift associated with the E isomer PL is observed for the 3-Z/E RT film, similar to the behavior in solution. The decreased absorbance and significantly suppressed PL upon thermal annealing are opposite to behavior in the shorter oligomers. The presence of the E isomer impacted optical properties much less in the 3-Z/E film compared to 1-Z/E and 2-Z/E. This is likely related to the lack of crystalline packing observed for E molecules in the 3-Z/E films.

Packing of molecules and nearest-neighbor interactions are the driving factors governing changes to solid-state optoelectronic behaviors. As molecules become sufficiently close (a few nanometers or less), coupling between transition dipole moments can occur, enabling new excited-state transitions. 53-55 This coupling depends on orientation of the transition dipole moments and therefore, molecular orientation and solid-state packing. The resultant effect on excited-state transitions outlined by Kasha has been described in terms of H-aggregates (often causing blue-shifts) and J-aggregates (red-Additional signatures of H-aggregates (or Jaggregates) often result in large (or minimal) Stokes shifts and suppressed (or enhanced) fluorescence. 55,56 A combination of both behaviors may also be observed in the case of Davydov splitting (DS), often seen in herringbone structures.<sup>34</sup> The possibility of charge transfer excitons also exist in crystal systems where molecules have significant electron wave function overlap. This is often seen in  $\pi$ -stacked systems and may also result in H- or J-like behavior depending on phase symmetry between the combination of lowest unoccupied

Table 2. Summary of Optical Properties from Solution and Thin-Film UV-Vis and PL Measurements<sup>a</sup>

	$\lambda_{\text{max,A}}$ (nm)	$\lambda_{\text{max,PL}}$ (nm)	$\Delta \lambda_{Stokes}$ (nm)	$\Delta A_{\mathrm{L/S}}$ (nm)	$\Delta PL_{L/S} \; (nm)$	$\Delta A_{Z/E}$ (nm)	$\Delta PL_{Z/E}$ (nm)
1-Z Solution	399	441	42				
1-Z/E Solution	413	450	37			14	9
1-Z RT	392	518	126	<b>-</b> 7	77		
1-Z/E RT	386	516	130	-27	66	-6	-2
1-Z TA	353	520	167	-46	79		
<b>1-</b> Z/E TA	383	514	131	-30	64	30	-6
2-Z Solution	476	550	74				
2-Z/E Solution	483	555	72			7	5
<b>2-</b> Z RT	392	611	219	-84	61		
<b>2-</b> Z/E RT	485	615	130	2	60	93	4
<b>2-</b> Z TA	425	609	184	-51	59		
<b>2-</b> Z/E TA	557	597	40	74	42	132	-12
3-Z Solution	510	627	117				
3-Z/E Solution	517	628	111			7	1
3-Z RT	503	657	154	<b>-</b> 7	30		
<b>3-</b> Z/E RT	497	661	164	-20	33	-6	4
<b>3-</b> Z TA	536	645	109	26	18		
3-Z/E TA	536	662	126	19	34	0	17

<sup>&</sup>quot;Peak values and spectral shifts are evaluated at the first excited-state transitions. Negative values indicate a blueshift.

molecular orbital and highest occupied molecular orbital states. These theories enable understanding of optical changes as one goes from miscible solutions to aggregates and the solid state.

The 1-Z RT film contains amorphous and crystalline regions evident from XRD and AFM. Larger separation and nonuniform dipole alignments in amorphous regions cause weak Coulomb coupling of transition dipole moments compared to the crystalline state. The herringbone nature of 1-Z crystallites and variety of nearest neighbor molecular pairs (Figure 5b) lends itself to Davydov Splitting (DS) with predominant Hbehavior observed by the blueshift in  $\lambda_{\text{max,A}}$ . Also, 1-Z film PL measurements show H-behavior evident by a large Stokes shift stemming from H-band absorption and subsequent emission from the J-band enabled by DS. Increased PL upon thermal annealing is attributed to J-band emission in the crystalline state. 1-E crystallites exhibit strong J-behavior evident by the long wavelength absorbance peak at ~473 nm. J-behavior is also seen in the increased intensity of fluorescence seen in the 1-Z/E TA film. Consistent with J-aggregates, minimal Stokes shift and preferred emission from the 0-0 transition occurs between E isomer absorbance and PL peaks, namely the 473 nm absorbance shoulder and 485 nm PL shoulder.

A variable spectral response dictated by isomer packing is further supported by 2-Z and 2-Z/E films with analogous trends seen for the Z and E crystallites. 2-Z crystallites possess DS with a predominant H-band seen in a blue-shifted  $\lambda_{\max,A}$ and a weak J-band producing a shoulder at ~535 nm. Interestingly, the 2-Z RT film has a larger blue-shift than the TA film, along with suppression of oscillator strength for the monomer transition at ~476 nm. Because minimal evidence of crystallites is present from AFM and XRD, short-range ordering (e.g., dimer formation) in amorphous regimes is the likely cause, leading to H-aggregate behavior in the absence of crystalline domains. Amorphous 2-E regimes exhibit a maximum absorbance only 2 nm red-shifted from the monomer absorbance. Annealing reveals strong J-behavior of 2-E crystallites evident by the large redshift in absorbance,  $\lambda_{\text{max,A}}$  occurring at the 0-0 transition, decreased Stokes shift, and increased PL intensity. Molecular packing was further

investigated and validated as the mechanism for these drastic spectral shifts by preparing solutions with varying weight percent ratios of  $\mathbf{2}\text{-}Z$  or  $\mathbf{2}\text{-}Z/E$  to inert polyvinylpyrrolidone-K30 (PVP). These solutions were spun into thin films, where PVP caused disrupted molecular packing of the bithiophene oligomers. As PVP concentration was increased, a gradual removal of intermolecular optical transitions was observed by UV—vis, eventually yielding absorbance profiles comparable to monomer transitions in  $\mathbf{2}\text{-}Z$  and  $\mathbf{2}\text{-}Z/E$  solution measurements (Figure S17).

The 3-Z and 3-Z/E films had minimal relative differences in absorbance spectra for RT and TA films. The additional octyl chain responsible for improving solubility seems to inhibit crystalline packing in RT films. Therefore, RT properties are governed largely by amorphous domains. Annealing results in suppressed PL, which would indicate H-aggregate formation and absence of J-bands from DS seen in the other compounds. Suppressed oscillator strength in the annealed 3-Z and 3-Z/E films may be caused by unfavorable orientation of transition dipole moments to incident electric fields. The minimal differences with E isomer concentration are attributed to lack of crystalline packing among E crystallites. Since no E crystallites were observed for the 3-Z/E film, coupling mechanisms that enable new optoelectronic transitions were largely absent.

Large differences between Z and E isomer films and deviation from monomer optical properties is seen because of the geometric isomer configurations, subsequent molecular packing, and resultant coupling mechanisms unique to the Z and E isomers. Predominant H-aggregate behavior was seen in Z crystallites, whereas J-behavior was seen in E crystallites, accounting for the observed thin-film absorbance and PL. The lack of close packing in the 3-Z/E films explained the similarity in observed behavior with its Z counterparts. Controlled molecular packing and resulting optoelectronic transitions by geometric isomers offers a means of varying the spectral range for photon collection in RCN based OPV devices. Additionally, the combination of Z and E crystallites for monoand bithiophene RCN derivatives lends itself to more favorable

ī

**ACS Applied Materials & Interfaces** 

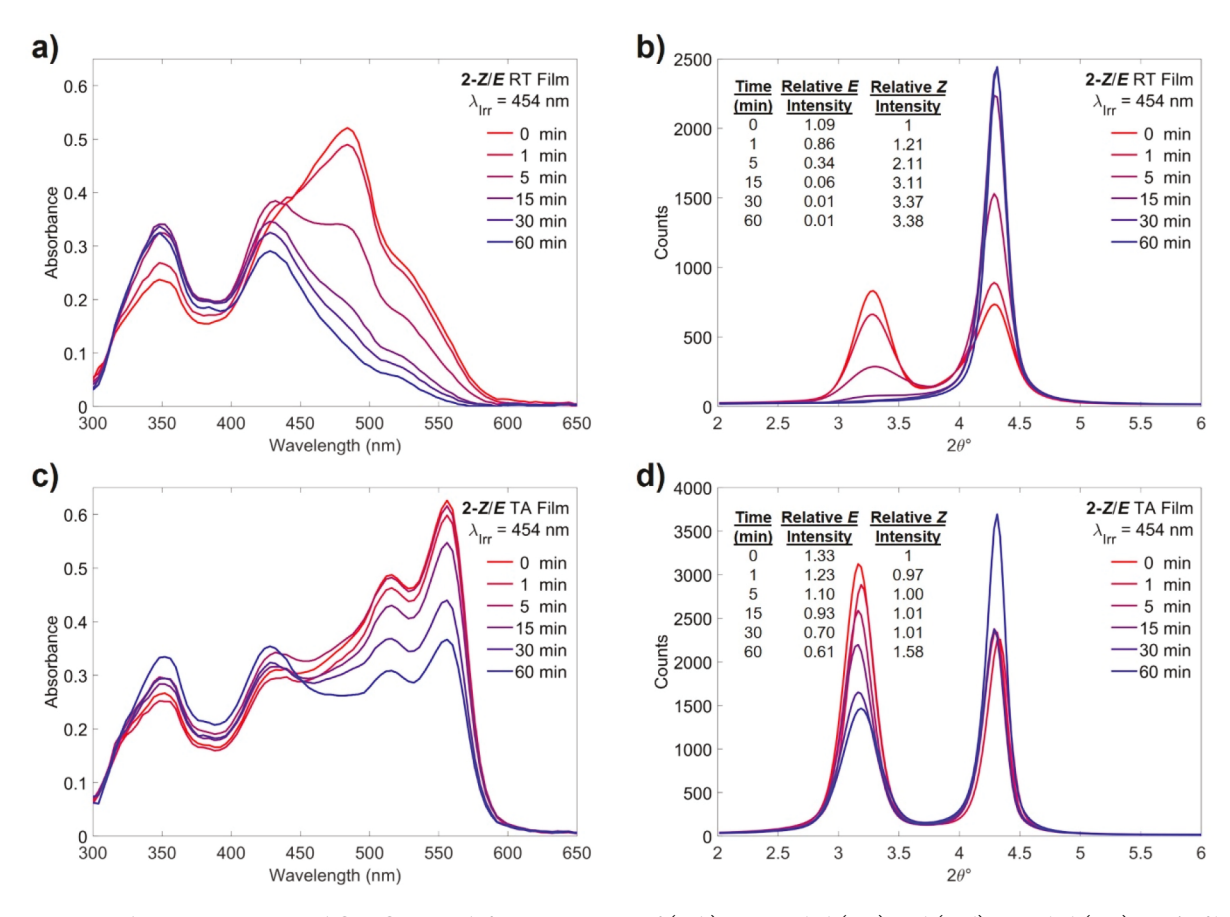


Figure 7. UV-vis absorption spectra and  $\Theta$ -2 $\Theta$  X-ray diffraction patterns of (a, b) unannealed (RT) and (c, d) annealed (TA) 2-Z/E films after 0-60 min of irradiation with blue light. Panels b and d contain tables for relative diffraction intensities, comparing maximum  $E(2\theta^\circ = 3.2^\circ)$  or  $Z(2\theta^\circ = 4.3^\circ)$  crystallite counts after irradiation relative to the diffraction intensity of the Z crystallite peak for the non-irradiated sample.

absorbance range for OPV applications compared to the pure Z films.

Isomerization in the Solid State. Because of the photoinduced configuration changes observed in solution, a solid-state investigation of isomer stability and photoswitching capability was carried out for the 2-Z and 2-Z/E oligomer films. Blue LED irradiation ( $\lambda_{irr}$  = 454 nm) and green LED irradiation ( $\lambda_{irr}$  = 523 nm) were used to irradiate 2-Z and 2-Z/ E thin films (both RT and TA films) to a photostationary state to investigate the possibility of photoisomerization in the solid state. After the irradiation experiments, films were dissolved in the solvent and examined using <sup>1</sup>H NMR spectroscopy to confirm and quantify isomer configuration (Figures S9 and \$10). Irradiation of pure 2-Z RT and 2-Z TA resulted in no detectable evidence of  $Z \rightarrow E$  isomerization based on postirradiation <sup>1</sup>H NMR analysis, evidenced by the lack of emergent signals associated with the 2-E form (Figure S12). This is attributed to spatial constraints as the *E* isomer requires expansion along the long molecular axis.

The  $E \to Z$  conversion, however, was observed in 2-Z/E RT and TA films by  $^1$ H NMR, UV-vis, and XRD analysis after light exposure. After 20 min of 454 nm irradiation,  $^1$ H NMR revealed 92% conversion of E isomers back to the Z configuration for RT films. This is compared to only 23% conversion for TA films (Figure S11). The UV-vis spectra also indicate significantly less  $E \to Z$  photoisomerization for TA films (Figure 7a, c). Nearly all absorbance contributions of the 2-E amorphous and crystalline regions are removed upon 60 min of blue LED irradiation of the 2-E/E RT film (Figure

7a). Absorption features intrinsic to the 2-E crystallites are reduced but still very pronounced in the 2-Z/E TA film after 60 min of irradiation. XRD patterns support these claims, with an intensity loss of the E-crystallite diffraction and increase in the Z-crystallite diffraction observed for these films upon irradiation (Figure 7b, d).

The loss of 99% diffraction intensity at a  $2\theta^{\circ}$  angle of  $3.2^{\circ}$ occurs by 30 min of irradiation in RT films, indicating loss of E crystallites (Figure 7b). Consistent with <sup>1</sup>H NMR and UV-vis, XRD shows thermally annealed samples were much less susceptible to light exposure, with 46% of the initial peak intensity at  $3.2^{\circ}$  still present for the 60 min irradiated 2-Z/E TA film (Figure 7d). The degree of Z isomer crystallinity was inversely affected by the irradiation process. Increased diffraction intensity at 4.3° for the RT film with irradiation indicates a photon-assisted crystallization of the 2-Z isomers. This resulted in a 3.38 factor increase in *Z* crystallite diffraction after 60 min of irradiation for the 2-Z RT film. This behavior. however, was not observed for 2-Z/E TA films between 0 and 30 min of irradiation, indicated by the stagnant intensity at 4.3°. This suggests, along with the stronger diffraction compared to non-irradiated RT films, that most Z isomers in the heat-treated films were already crystalline. The delayed onset and sudden rise in intensity for the 60 min 2-Z/E TA film at 4.3° is attributed to photoinduced crystallization of the newly formed Z isomers from the  $E \rightarrow Z$  conversion process. The delayed onset may be explained by limited nearest neighbor Z-isomers. Newly converted Z-isomers from an E crystallite would be nearest to E-isomers until enough nearest

neighbors are also photoisomerized. When a critical concentration of isomers is converted, long-range order, Z-crystallites may form. In the RT sample, enough amorphous Z isomers were already present to enable immediate photoinduced Z-crystallization.

An analogue  $^1$ H NMR study was performed with green (523 nm) light exposure and also exhibited  $E \rightarrow Z$  photoisomerization along with lesser conversion in thermally annealed films (Figure S10). Furthermore, the solid-state photoisomerization was probed using 454 nm light in conjunction to simultaneous heat exposure of 60  $^{\circ}$ C. The 2-Z/E RT and 2-Z/E TA films lost all spectral features related to the E-isomer before 1 and 3 min, respectively (Figure S13). Therefore, the thermodynamic contribution to solid-state photoisomerization is of fundamental importance to film stability. In all cases, consistent with increased crystallinity of 2-E domains upon thermal annealing, tight packing of 2-E molecules presents greater spatial constraints that impede isomerization, thus increasing the photostability of the E isomers.

### CONCLUSION

This work demonstrates that double-bond isomerization in  $\pi$ conjugated donor-acceptor oligomers can have a significant impact on molecular packing in the solid state, affecting the morphology and crystal structures, which in turn have strong consequences on the optical characteristics of the organic electronic thin films. Three dicyanorhodanine-functionalized thiophene oligomer model substrates (1-Z, 2-Z, and 3-Z) were synthesized, and gram-scale isomerization reactions were performed to yield solid-state Z/E mixtures (1-Z/E, 2-Z/E, and 3-Z/E) with a varying E content of 25, 53, and 45%, respectively. In solution, the presence of *E* isomers resulted in a slight redshift and increase in the UV-vis absorption. Decreased photoluminescence intensity was observed for Z/ E mixtures compared to the pure Z form for compounds 2 and 3, whereas the changes between compound 1-Z and 1-Z/Ewere less drastic. Consequences of E-isomer composition manifested in the solid state, impacting surface morphology, molecular packing, and subsequent optical properties. Atomic force microscopy and X-ray diffraction of spin-coated thin films revealed surface morphology and crystallite packing preferences of pure Z isomers and Z/E mixtures. Correlating molecular packing behaviors to their optical absorption and PL spectra, we found that optical transitions of these compounds are extremely sensitive to neighboring environments and molecular packing arrangement. This is best illustrated by the platelet (2-Z) and fiber-shaped (2-E) morphologies of their respective crystallites in thin films, along with the ~7 Å increase in the interplanar spacing for the E crystallites, and the 132 nm difference in the peak absorption wavelength between the 2-Z TA and 2-Z/E TA films. Solid-state isomerization experiments were performed via irradiation of Z isomer and Z/E thin films to gauge the extent of photoswitching in the solid state. Although  $Z \rightarrow E$  isomerization was not observed under prolonged irradiation, the reverse reaction  $(E \rightarrow Z)$  was observed upon irradiation of 2-Z/E mixture thin films, with the rate of conversion dependent on the degree of crystallinity. Looking forward, on the basis of the knowledge gained through this work, one could imagine prescribed, wellcontrolled photoisomerization processes included in the arsenal of approaches already used to optimize optoelectronic

thin-film morphology and properties. Work along these lines is continuing in our laboratories.

#### METHODS

Material Synthesis. The synthesis of all intermediates and final RCN-functionalized target molecules are shown in the Supporting Information (pages S3 and S4). Compounds 1-Z and 2-Z were synthesized according to the literature precedent (Scheme S1),<sup>25</sup> and compound 3-Z was synthesized using a similar strategy (Scheme S2). In all cases, the final RCN-functionalized target molecules (1-Z, 2-Z, and 3-Z) were isolated, with the Z form being the only detectable isomer resulting from the synthesis. The structural integrity of all known compounds was confirmed by <sup>1</sup>H and <sup>13</sup>C NMR (pages S4-S14 in the Supporting Information) with further characterization by high-resolution mass spectrometry (HRMS). To acquire solid-state samples comprising Z/E mixtures for compounds 1, 2, and 3, we conducted gram-scale isomerization experiments, and the general procedure is outlined in the Supporting Information (pages S14 and S15). Approximately 1.0 g of each synthesized target molecule (1-Z, 2-Z, and 3-Z) was dissolved in chloroform (200 mL) and each solution was irradiated at the appropriate wavelength to result in a unique Z/E distribution at the photostationary state (see Figure S1 for more information on irradiation sources). The solvent was removed, and the solid-state samples were dried prior to <sup>1</sup>H NMR analysis to determine the final Z/E isomeric ratio for each sample. The final isomeric ratios for 1-Z/E, 2-Z/E, and 3-Z/E were determined by <sup>1</sup>H NMR to be 75/25 (Figure S2), 47/53 (Figure S3), and 55/45 (Z/E) (Figure S4), respectively. Each pure Z sample (1-Z, 2-Z, and 3-Z) was compared with the corresponding solid-state isomeric mixtures (1-Z/E, 2-Z/E, and 3-Z/E) for the following characterizations.

Thin-Film Fabrication. Thin films were fabricated inside a glovebox with a nitrogen environment, using a spin coating process. The investigated compounds were taken in their powder form and dissolved in chlorobenzene with concentrations of 30 mg/mL. They were dynamically casted with a spin speed of 2000 rpm for 60 s on glass substrates containing a spin-coated poly(3,4-ethylenedioxythiophene) polystyrenesulfonate (PEDOT:PSS) layer (approximately 25 nm thick) to improve wettability. Thermal annealing experiments were carried out for some samples by placing them on a hot plate held at 90 °C for 1 h. Light exposure was minimized during each step of the process and samples were stored in the dark.

Thin-Film Optical Absorption Measurements. A 100 W quartz tungsten halogen lamp was used in conjunction with a Cornerstone 260 1/4 m monochromator (Newport 74100) to generate monochromatic light. The incident light was chopped at 480 Hz and recorded with a Newport 818-UV photodetector connected to a current amplifier (Keithley 428) and lock-in amplifier (Stanford Research Systems SR830 DSP). Transmittance and reflectance of thin-film samples were measured simultaneously, which were used to calculate the thin-film absorbance. Monochromator slit widths were adjusted to enable 3 nm resolution in spectral measurements.

Photoluminescence. Photoluminescence was measured with a Jasco FP-6500 spectrofluorometer. Solution PL was conducted on 20  $\mu$ M solutions dissolved in chloroform with excitation wavelengths of 375, 475, and 510 nm for compounds 1, 2, and 3, respectively. Solutions and films were kept in the dark until measurements were performed. PL measurements were normalized by excitation wavelength absorptance and to a global maximum emission among the Z and Z/E solutions. Thin-film PL was measured at excitation wavelengths of 360, 420, and 515 nm for compounds 1, 2, and 3, respectively. Excitation wavelengths were chosen for thin films at wavelengths with similar absorbance behavior between Z and Z/E films. PL measurements were normalized by their absorptance at the excitation wavelength and to the global maximum emission among the Z and Z/E RT and TA films to make comparisons on PL efficiency between isomers.

Atomic Force Microscopy. Atomic force microscopy (AFM) was carried out using a Dimension 3100 AFM operated in the tapping

mode at 325 kHz. An aluminum-coated silicon tip (Umasch HQ:NSC15/AL BS) was utilized for imaging.

X-ray Diffraction. All diffraction studies were performed on a Malvern Panalytical's X'Pert Pro MRD system employing the Bragg-Brentano diffraction geometry using a Cu  $K_{\alpha}$  X-ray source. A parabolic mirror forming a quasi-parallel beam was used in conjunction with a 1/16° divergent slit and a 15 mm beam-width mask to inhibit beam spill. A 5 mm beam width mask was used in pole figure measurements to further limit beam spill upon sample tilting. Diffraction beam optics consisted of a point detector, a 0.27° parallel plate collimator, and a 0.1 mm width receiving slit to improve resolution for low  $2\Theta$  angles. A proportional Xe point detector was used to measure diffracted intensity. A line profile analysis software (LIPRAS)<sup>59</sup> was used to fit diffraction peaks and calculate peak parameters. Pole figures were conducted for sample tilt from 0-90° and azimuthal angle of 0-355° using an out-of-plane pole figure geometry with a 5° step size for the angles. Sample background corrections were measured at a  $2\Theta$  value of  $\sim 1^{\circ}$  relative to the diffracting plane.

Solid-State Photoisomerization. Thin films of compounds 2-Z and 2-Z/E were prepared as described previously, using either RT or TA processing conditions. RT and TA thin films were irradiated at a 454 or 523 nm wavelength in a glovebox using the same LED sources used for the gram-scale photoisomerization (Figures S1 and S8). LED irradiation intensity during exposure was 10.9 and 3.0 mW/cm² for the blue and green LEDs, respectively. Non-irradiated thin films were stored in the dark during exposure to prohibit unwanted photoisomerization. Optical characterization of the films was performed immediately after irradiation.

## ASSOCIATED CONTENT

# **Supporting Information**

The Supporting Information is available free of charge at https://pubs.acs.org/doi/10.1021/acsami.2c05946.

Synthesis and structural characterization details, computational data summaries and details, gram-scale isomerization experiments and NMR data, solid-state isomerization NMR data, thermogravimetric analysis (TGA), irradiation sources, and computational details (PDF)

# AUTHOR INFORMATION

## **Corresponding Authors**

Ronald K. Castellano — Department of Chemistry, University of Florida, Gainesville, Florida 32611, United States; orcid.org/0000-0003-4322-9932; Email: castellano@chem.ufl.edu

Jiangeng Xue — Department of Materials Science and Engineering, University of Florida, Gainesville, Florida 32611, United States; Email: jxue@mse.ufl.edu

## **Authors**

David M. Camero – Department of Materials Science and Engineering, University of Florida, Gainesville, Florida 32611, United States; © orcid.org/0000-0001-5411-2575

Nathan J. Grinalds – Department of Materials Science and Engineering, University of Florida, Gainesville, Florida 32611, United States

Cory T. Kornman – Department of Chemistry, University of Florida, Gainesville, Florida 32611, United States

Stefano Barba — Department of Materials Science and Engineering, University of Florida, Gainesville, Florida 32611, United States; orcid.org/0000-0002-8952-4462

Lei Li – Department of Chemistry, University of Florida, Gainesville, Florida 32611, United States; Department of Materials Science and Engineering, Center for Optical Materials Science and Engineering Technologies (COMSET), Clemson University, Clemson, South Carolina 29634, United States; orcid.org/0000-0001-8901-4932

Asmerom O. Weldeab — Department of Chemistry, University of Florida, Gainesville, Florida 32611, United States;
orcid.org/0000-0002-3004-7841

Complete contact information is available at: https://pubs.acs.org/10.1021/acsami.2c05946

#### **Author Contributions**

The manuscript was written through contributions of all authors. All authors have given approval to the final version of the manuscript.

# **Funding**

R.K.C. and J.X. are thankful to the National Science Foundation for supporting this research (CHE-1507561 and CHE-1904534). The mass spectrometric data were obtained by the UF Department of Chemistry Mass Spectrometry Research and Education Center supported, in part, by the National Institutes of Health (NIH S10OD021758-01A1).

#### Note

The authors declare no competing financial interest.

#### ACKNOWLEDGMENTS

Acknowledgment is made to National Science Foundation for funding support of this research (CHE-1507561 and CHE-1904534). C.T.K. wishes to acknowledge the University of Florida (UF) Department of Chemistry for providing a Graduate School Fellowship (GSF), which made this research possible. We acknowledge the University of Florida Research Computing for providing computational resources and support that have contributed to the research results reported in this publication (https://www.rc.ufl.edu). The mass spectrometric data were obtained by the UF Department of Chemistry Mass Spectrometry Research and Education Center supported, in part, by the National Institutes of Health (NIH S10OD021758-01A1). We also thank the UF Center for Nuclear Magnetic Resonance Spectroscopy for providing equipment and support that have contributed to these published results.

## REFERENCES

- (1) Forrest, S. R. The Path to Ubiquitous and Low-Cost Organic Electronic Appliances on Plastic. *Nature* **2004**, 428, 911–918.
- (2) Zheng, Y.; Xue, J. Organic Photovoltaic Cells Based on Molecular Donor-Acceptor Heterojunctions. *Polym. Rev.* **2010**, *50*, 420–453.
- (3) Xue, J. Perspectives on Organic Photovoltaics. *Polym. Rev.* **2010**, 50, 411–419.
- (4) Ng, L. W. T.; Lee, S. W.; Chang, D. W.; Hodgkiss, J. M.; Vak, D. Organic Photovoltaics' New Renaissance: Advances toward Roll-to-Roll Manufacturing of Non-Fullerene Acceptor Organic Photovoltaics. *Adv. Mater. Technol. (Weinheim, Ger.)* **2022**, 2101556.
- (5) Meng, D.; Zheng, R.; Zhao, Y.; Zhang, E.; Dou, L.; Yang, Y. Near-Infrared Materials: The Turning Point of Organic Photovoltaics. *Adv. Mater.* **2022**, *34*, 2107330.
- (6) Gao, H.-H.; Sun, Y.; Cai, Y.; Wan, X.; Meng, L.; Ke, X.; Li, S.; Zhang, Y.; Xia, R.; Zheng, N.; Xie, Z.; Li, C.; Zhang, M.; Yip, H.-L.; Cao, Y.; Chen, Y. Achieving Both Enhanced Voltage and Current through Fine-Tuning Molecular Backbone and Morphology Control in Organic Solar Cells. *Adv. Energy Mater.* **2019**, *9*, 1901024.
- (7) Zhu, L.; Zhang, M.; Zhou, G.; Hao, T.; Xu, J.; Wang, J.; Qiu, C.; Prine, N.; Ali, J.; Feng, W.; Gu, X.; Ma, Z.; Tang, Z.; Zhu, H.; Ying, L.; Zhang, Y.; Liu, F. Efficient Organic Solar Cell with 16.88%

- Efficiency Enabled by Refined Acceptor Crystallization and Morphology with Improved Charge Transfer and Transport Properties. *Adv. Energy Mater.* **2020**, *10*, 1904234.
- (8) Chang, M.; Meng, L.; Wang, Y.; Ke, X.; Yi, Y.-Q.-Q.; Zheng, N.; Zheng, W.; Xie, Z.; Zhang, M.; Yi, Y.; Zhang, H.; Wan, X.; Li, C.; Chen, Y. Achieving an Efficient and Stable Morphology in Organic Solar Cells via Fine-Tuning the Side Chains of Small-Molecule Acceptors. *Chem. Mater.* **2020**, *32*, 2593–2604.
- (9) Li, S.; Li, C.-Z.; Shi, M.; Chen, H. New Phase for Organic Solar Cell Research: Emergence of Y-Series Electron Acceptors and Their Perspectives. ACS Energy Lett. 2020, 5, 1554–1567.
- (10) Dey, S. Recent Progress in Molecular Design of Fused Ring Electron Acceptors for Organic Solar Cells. Small 2019, 15, 1900134.
- (11) Chatterjee, S.; Jinnai, S.; Ie, Y. Nonfullerene Acceptors for P3HT-Based Organic Solar Cells. *J. Mater. Chem. A* **2021**, 9, 18857—18886.
- (12) Lu, B.; Zhang, Z.; Wang, J.; Cai, G.; Wang, J.; Yuan, X.; Ding, Y.; Wang, Y.; Yao, Y. Nonfullerene Electron Acceptors with Electron-Deficient Units Containing Cyano Groups for Organic Solar Cells. *Mater. Chem. Front.* **2021**, *5*, 5549–5572.
- (13) Xiao, B.; Du, M.; Wang, X.; Xiao, Z.; Li, G.; Tang, A.; Ding, L.; Geng, Y.; Sun, X.; Zhou, E. Effects of Oxygen Atoms Introduced at Different Positions of Non-Fullerene Acceptors in the Performance of Organic Solar Cells with Poly(3-hexylthiophene). ACS Appl. Mater. Interfaces 2020, 12, 1094–1102.
- (14) Lin, Y.; Wang, J.; Zhang, Z.-G.; Bai, H.; Li, Y.; Zhu, D.; Zhan, X. An Electron Acceptor Challenging Fullerenes for Efficient Polymer Solar Cells. *Adv. Mater.* **2015**, *27*, 1170–1174.
- (15) Duan, T.; Chen, Q.; Yang, Q.; Hu, D.; Cai, G.; Lu, X.; Lv, J.; Song, H.; Zhong, C.; Liu, F.; Yu, D.; Lu, S. Simple Thiazole-Centered Oligothiophene Donor Enables 15.4% Efficiency All Small Molecule Organic Solar Cells. *J. Mater. Chem. A* **2022**, *10*, 3009–3017.
- (16) Liu, Q.; Jiang, Y.; Jin, K.; Qin, J.; Xu, J.; Li, W.; Xiong, J.; Liu, J.; Xiao, Z.; Sun, K.; Yang, S.; Zhang, X.; Ding, L. 18% Efficiency Organic Solar Cells. *Sci. Bull.* **2020**, *65*, 272–275.
- (17) Liu, F.; Zhou, L.; Liu, W.; Zhou, Z.; Yue, Q.; Zheng, W.; Sun, R.; Liu, W.; Xu, S.; Fan, H.; Feng, L.; Yi, Y.; Zhang, W.; Zhu, X. Organic Solar Cells with 18% Efficiency Enabled by an Alloy Acceptor: A Two-in-One Strategy. Adv. Mater. 2021, 33, 2100830.
- (18) Hedley, G. J.; Ruseckas, A.; Samuel, I. D. W. Light Harvesting for Organic Photovoltaics. *Chem. Rev.* **2017**, *117*, 796–837.
- (19) Dudem, B.; Jung, J. W.; Yu, J. S. Improved Light Harvesting Efficiency of Semitransparent Organic Solar Cells Enabled by Broadband/Omnidirectional Subwavelength Antireflective Architectures. J. Mater. Chem. A 2018, 6, 14769–14779.
- (20) El-Zohry, A.; Orthaber, A.; Zietz, B. Isomerization and Aggregation of the Solar Cell Dye D149. *J. Phys. Chem. C* **2012**, 116, 26144–26153.
- (21) El-Zohry, A. M.; Zietz, B. Concentration and Solvent Effects on the Excited State Dynamics of the Solar Cell Dye D149: The Special Role of Protons. *J. Phys. Chem. C* **2013**, *117*, 6544–6553.
- (22) Zietz, B.; Gabrielsson, E.; Johansson, V.; El-Zohry, A. M.; Sun, L.; Kloo, L. Photoisomerization of the Cyanoacrylic Acid Acceptor Group A Potential Problem for Organic Dyes in Solar Cells. *Phys. Chem. Chem. Phys.* **2014**, *16*, 2251–2255.
- (23) Bi, P.; Zhang, S.; Wang, J.; Ren, J.; Hou, J. Progress in Organic Solar Cells: Materials, Physics and Device Engineering. *Chin. J. Chem.* **2021**, *39*, 2607–2625.
- (24) Zhao, C.; Guo, Y.; Zhang, Y.; Yan, N.; You, S.; Li, W. Diketopyrrolepyrrole-Based Conjugated Materials for Non-Fullerene Organic Solar Cells. *J. Mater. Chem. A* **2019**, *7*, 10174–10199.
- (25) Kornman, C. T.; Li, L.; Weldeab, A. O.; Ghiviriga, I.; Abboud, K. A.; Castellano, R. K. Photoisomerization of Dicyanorhodanine-Functionalized Thiophenes. *Chem. Sci.* **2020**, *11*, 10190–10197.
- (26) Che, Y.; Niazi, M. R.; Izquierdo, R.; Perepichka, D. F. Mechanism of the Photodegradation of A-D-A Acceptors for Organic Photovoltaics. *Angew. Chem., Int. Ed.* **2021**, *60*, 24833–24837.
- (27) Cui, Y.; Xu, Y.; Yao, H.; Bi, P.; Hong, L.; Zhang, J.; Zu, Y.; Zhang, T.; Qin, J.; Ren, J.; Chen, Z.; He, C.; Hao, X.; Wei, Z.; Hou, J.

- Single-Junction Organic Photovoltaic Cell with 19% Efficiency. Adv. Mater. 2021, 33, 2102420.
- (28) Liu, Z.-X.; Yu, Z.-P.; Shen, Z.; He, C.; Lau, T.-K.; Chen, Z.; Zhu, H.; Lu, X.; Xie, Z.; Chen, H.; Li, C.-Z. Molecular Insights of Exceptionally Photostable Electron Acceptors for Organic Photovoltaics. *Nat. Commun.* **2021**, *12*, 3049.
- (29) Wienk, M. M.; Kroon, J. M.; Verhees, W. J. H.; Knol, J.; Hummelen, J. C.; van Hal, P. A.; Janssen, R. A. J. Efficient Methano[70]Fullerene/MDMO-PPV Bulk Heterojunction Photovoltaic Cells. *Angew. Chem., Int. Ed.* **2003**, 42, 3371–3375.
- (30) Umeyama, T.; Igarashi, K.; Sakamaki, D.; Seki, S.; Imahori, H. Unique Cohesive Nature of the  $\beta_1$ -Isomer of [70]PCBM Fullerene on Structures and Photovoltaic Performances of Bulk Heterojunction Films with PffBT4T-2OD Polymers. *Chem. Commun. (Cambridge, U. K.)* **2018**, *54*, 405–408.
- (31) Zhao, D.; Wu, Q.; Cai, Z.; Zheng, T.; Chen, W.; Lu, J.; Yu, L. Electron Acceptors Based on  $\alpha$ -Substituted Perylene Diimide (PDI) for Organic Solar Cells. *Chem. Mater.* **2016**, 28, 1139–1146.
- (32) Wang, J.; Zhang, J.; Xiao, Y.; Xiao, T.; Zhu, R.; Yan, C.; Fu, Y.; Lu, G.; Lu, X.; Marder, S. R.; Zhan, X. Effect of Isomerization on High-Performance Nonfullerene Electron Acceptors. *J. Am. Chem. Soc.* **2018**, *140*, 9140–9147.
- (33) Yang, Y.; Zhang, Z.-G.; Bin, H.; Chen, S.; Gao, L.; Xue, L.; Yang, C.; Li, Y. Side-Chain Isomerization on an n-Type Organic Semiconductor ITIC Acceptor Makes 11.77% High Efficiency Polymer Solar Cells. *J. Am. Chem. Soc.* **2016**, *138*, 15011–15018.
- (34) Chen, Y.; Wan, X.; Long, G. High Performance Photovoltaic Applications Using Solution-Processed Small Molecules. *Acc. Chem. Res.* **2013**, *46*, 2645–2655.
- (35) Savikhin, V.; Babics, M.; Neophytou, M.; Liu, S.; Oosterhout, S. D.; Yan, H.; Gu, X.; Beaujuge, P. M.; Toney, M. F. Impact of Polymer Side Chain Modification on OPV Morphology and Performance. *Chem. Mater.* **2018**, *30*, 7872–7884.
- (36) Ma, L.; Yao, H.; Wang, J.; Xu, Y.; Gao, M.; Zu, Y.; Cui, Y.; Zhang, S.; Ye, L.; Hou, J. Impact of Electrostatic Interaction on Bulk Morphology in Efficient Donor–Acceptor Photovoltaic Blends. *Angew. Chem., Int. Ed.* **2021**, *60*, 15988–15994.
- (37) Du, Z.; Chen, W.; Chen, Y.; Qiao, S.; Bao, X.; Wen, S.; Sun, M.; Han, L.; Yang, R. High Efficiency Solution-Processed Two-Dimensional Small Molecule Organic Solar Cells Obtained via Low-Temperature Thermal Annealing. *J. Mater. Chem. A* **2014**, *2*, 15904—15911.
- (38) Stupp, S. I.; Palmer, L. C. Supramolecular Chemistry and Self-Assembly in Organic Materials Design. *Chem. Mater.* **2014**, *26*, 507–518.
- (39) Grand, C.; Zajaczkowski, W.; Deb, N.; Lo, C. K.; Hernandez, J. L.; Bucknall, D. G.; Müllen, K.; Pisula, W.; Reynolds, J. R. Morphology Control in Films of Isoindigo Polymers by Side-Chain and Molecular Weight Effects. ACS Appl. Mater. Interfaces 2017, 9, 13357–13368.
- (40) Cao, X.; Liu, X.; Chen, L.; Mao, Y.; Lan, H.; Yi, T. Photoisomerization-Induced Morphology and Transparency Transition in an Azobenzene Based Two-Component Organogel System. *J. Colloid Interface Sci.* **2015**, 458, 187–193.
- (41) Wang, R.; Jiang, L.; Iyoda, T.; Tryk, D. A.; Hashimoto, K.; Fujishima, A. Investigation of the Surface Morphology and Photoisomerization of an Azobenzene-Containing Ultrathin Film. *Langmuir* 1996, 12, 2052–2057.
- (42) Markiewicz, G.; Pakulski, D.; Galanti, A.; Patroniak, V.; Ciesielski, A.; Stefankiewicz, A. R.; Samori, P. Photoisomerisation and Light-Induced Morphological Switching of a Polyoxometalate—Azobenzene Hybrid. *Chem. Commun. (Cambridge, U. K.)* **2017**, 53, 7278–7281.
- (43) Leistner, A.-L.; Pianowski, Z. Smart Photochromic Materials Triggered with Visible Light. *Eur. J. Org. Chem.* **2022**, 2022, e202101271.
- (44) Hou, L.; Zhang, X.; Cotella, G. F.; Carnicella, G.; Herder, M.; Schmidt, B. M.; Pätzel, M.; Hecht, S.; Cacialli, F.; Samorì, P. Optically

- Switchable Organic Light-Emitting Transistors. *Nat. Nanotechnol.* **2019**, *14*, 347–353.
- (45) Li, Z.; Liu, X.; Wang, G.; Li, B.; Chen, H.; Li, H.; Zhao, Y. Photoresponsive Supramolecular Coordination Polyelectrolyte as Smart Anticounterfeiting Inks. *Nat. Commun.* **2021**, *12*, 1363.
- (46) Yamaguchi, H.; Kobayashi, Y.; Kobayashi, R.; Takashima, Y.; Hashidzume, A.; Harada, A. Photoswitchable Gel Assembly Based on Molecular Recognition. *Nat. Commun.* **2012**, *3*, 603.
- (47) Peng, L.; You, M.; Yuan, Q.; Wu, C.; Han, D.; Chen, Y.; Zhong, Z.; Xue, J.; Tan, W. Macroscopic Volume Change of Dynamic Hydrogels Induced by Reversible DNA Hybridization. *J. Am. Chem. Soc.* **2012**, *134*, 12302–12307.
- (48) Yu, S. H.; Hassan, S. Z.; Nam, G.-H.; An, S.; Kang, B.; Chung, D. S. Consideration of Azobenzene-Based Self-Assembled Monolayer Deposition Conditions for Maximizing Optoelectronic Switching Performances. *Chem. Mater.* **2021**, *33*, 5991–6002.
- (49) Sing, W. T.; Lee, C. L.; Yeo, S. L.; Lim, S. P.; Sim, M. M. Arylalkylidene Rhodanine with Bulky and Hydrophobic Functional Group as Selective HCV NS3 Protease Inhibitor. *Bioorg. Med. Chem. Lett.* **2001**, *11*, 91–94.
- (50) Behera, S. K.; Park, S. Y.; Gierschner, J. Dual Emission: Classes, Mechanisms, and Conditions. *Angew. Chem., Int. Ed.* **2021**, *60*, 22624–22638.
- (51) Kukhta, N. A.; Bryce, M. R. Dual Emission in Purely Organic Materials for Optoelectronic Applications. *Mater. Horiz.* **2021**, *8*, 33–55
- (52) Lin, R.; Galili, M.; Quaade, U. J.; Brandbyge, M.; Bjørnholm, T.; Esposti, A. D.; Biscarini, F.; Stokbro, K. Spontaneous Dissociation of a Conjugated Molecule on the Si(100) Surface. *J. Chem. Phys.* **2002**, *117*, 321–330.
- (53) McRae, E. G.; Kasha, M. Enhancement of Phosphorescence Ability Upon Aggregation of Dye Molecules. *J. Chem. Phys.* **1958**, 28, 721–722.
- (54) Kasha, M. Energy Transfer Mechanisms and the Molecular Exciton Model for Molecular Aggregates. *Radiat. Res.* **1963**, *20*, 55–70.
- (55) Kasha, M.; Rawls, H. R.; Ashraf El-Bayoumi, M. The Exciton Model in Molecular Spectroscopy. *Pure Appl. Chem.* **1965**, *11*, 371–392
- (56) Hestand, N. J.; Spano, F. C. Expanded Theory of H- and J-Molecular Aggregates: The Effects of Vibronic Coupling and Intermolecular Charge Transfer. *Chem. Rev.* **2018**, *118*, 7069–7163.
- (57) Merrifield, R. E. Ionized States in a One-Dimensional Molecular Crystal. *J. Chem. Phys.* **1961**, *34*, 1835–1839.
- (58) Bulović, V.; Burrows, P. E.; Forrest, S. R.; Cronin, J. A.; Thompson, M. E. Study of Localized and Extended Excitons in 3,4,9,10-Perylenetetracarboxylic Dianhydride (PTCDA) I. Spectroscopic Properties of Thin Films and Solutions. *Chem. Phys.* **1996**, 210, 1–12.
- (59) Esteves, G.; Ramos, K.; Fancher, C.; Jones, J. LIPRAS: Line-Profile Analysis Software; 2017.